

# A Numerical Study on Hydrogen Jet Flame Combustion in MILD Conditions

Karl Planke\*, Federica Farisco†, Felix Grimm‡, and Andreas Huber§  
*Deutsches Zentrum für Luft- und Raumfahrt, German Aerospace Center (DLR),  
Institute of Combustion Technology, Stuttgart, Germany, 70569*

A large degree of dilution and high temperatures are what characterizes MILD (Moderate or Intense Low oxygen Dilution) combustion. This regime is commonly prevailing in FLOX® systems, where hot gases are recirculated in order to stabilize the combustion process. Current technical developments in the fight against climate change require combustion systems to run with high calorific and at the same time clean fuels, like hydrogen in particular. However, certain difficulties arise in the design process of energy conversion systems with the use of hydrogen. Especially in modeling and simulation, the choice of chemical reaction mechanisms and combustion models is critical. Therefore, in the present study, a jet flame test case is thoroughly investigated, mimicking a combustion situation that is present in FLOX® based burners. Several reaction schemes and models are tested and results are validated with a large experimental data set. This study features an elaborate investigation of reaction schemes usable in combustor design phases and assesses their applicability in the leaner combustion regime to provide guidance for the design of hydrogen-based combustion systems for energy and aviation applications.

## I. Introduction

In order to reduce nitrogen oxide ( $\text{NO}_x$ ) emissions of recent heavy-duty gas turbines and aeroengines, conducting combustion under lean premixed conditions became the most adopted of all technologies available. However, since thermoacoustic instabilities and flashback might arise in these combustion systems, the FLOX® (flameless oxidation) concept was developed as an alternative burner design strategy to mitigate climate change. Operating in the MILD regime (Moderate or Intense Low oxygen Dilution) of combustion, FLOX® systems were first applied in low calorific atmospheric furnaces [1]. For later adaptations, featuring rather discrete flames, the term recirculation-stabilized jet flame (RSJF) combustion is also used. Under MILD conditions, flow field properties and flame stabilization are characterized by hot combustion products being recirculated upstream, where they dilute the oxidizer stream to be mixed with unburned fuel. Compared to conventional combustor systems, typically a more uniform temperature distribution is achieved, which leads to reduced  $\text{NO}_x$  emissions [2]. Further experimental [3] and numerical [4] work was performed to analyze the MILD combustion of gaseous fuels.

Concerning the FLOX® concept specifically, fuel and air are injected through two coaxially arranged nozzles, where the air stream is surrounding the fuel jet. A FLOX® burner typically features several injection positions forming a circular pattern around its central axis. When entering the combustion chamber, fuel and air come into contact being mixed into recirculated combustion products from downstream. These hot gases help ignite the fresh mixture of fuel and air upstream at the flame root. During stationary operation, characteristic inner and outer recirculation zones are formed along the central axis and combustion chamber walls respectively. As a result, nearly homogeneous temperature distributions, large ranges of stable operating points and low emissions [5, 6] can be achieved, outlining the main features of FLOX® systems. Additionally, the presence of jets with high velocity and momentum reduces the flashback risk, which promotes this burner design for multi-fuel applications including hydrogen combustion [7, 8]. To date, experimental [9] and numerical [10] research on the flame dynamics of FLOX® burners resulted in an increased operational range and adaptations for different applications. In order to apply the FLOX® concept to combustion chambers for modern gas turbines, a deep understanding of the jet flame stabilization mechanisms and influence of the fuel [11] is fundamental.

---

\*Research Associate / PhD student, Combustion Chamber Development, karl.planke@dlr.de

†Research Associate, Combustion Chamber Development, federica.farisco@dlr.de

‡Group Leader and Research Associate, Combustion Chamber Development

§Head of the DLR Institute of Combustion Technology

Seeking to support the development of MILD operated combustion systems for clean and high calorific fuels, this paper focuses on hydrogen combustion. Currently, the numerical simulation of lifted turbulent hydrogen flames is a challenging task, because of the complex turbulence-chemistry interaction. Sufficient knowledge concerning both up-to-date numerical modeling and experimental techniques is still missing in order to allow for a reliable prediction of combustor capabilities. The outcomes of this paper could be used as a baseline for the further development of industrial applications. The experimental reference case was chosen since it features MILD conditions comparable to those expected in a FLOX<sup>®</sup> system. All simulations were performed within the Reynolds-Averaged Navier–Stokes (RANS) framework as it is the current standard tool for industrial design processes. While still capturing the main characteristics of the fluid dynamics, computational effort is significantly reduced compared to methods like Large Eddy Simulation (LES) or Detached Eddy Simulation (DES). Regarding combustion modeling, the Eddy Dissipation Model (EDM) by Magnussen and Hjertager [12] was applied in combination with its extension, the Eddy Dissipation Concept (EDC) by Magnussen [13], which includes detailed chemical kinetics for turbulent reacting flows.

This paper is structured as follows: Opening with preliminary considerations, the next section explains the underlying experimental reference cases in detail. Subsequently, a numerical setup is derived by determining suitable boundary conditions. In order to evaluate the numerical model, results for non-reacting flow simulations are analyzed considering several parameters, including a mesh independence study. Based on this, the results of reacting-flow simulations featuring different chemical reaction mechanisms are presented. The predicted lift-off heights are discussed and compared with experimental data from literature. In the concluding section, a brief summary of results is given as well as an outlook on possible topics of further research.

## II. Experimental Reference Cases

Several authors have presented experimental and numerical investigations related to hydrogen combustion. Cabra et al. [14] provided the first experimental results for lifted hydrogen flames in a co-flow. They also numerically predicted the lift-off height for a single co-flow temperature using a probability density function (PDF) and the EDC as combustion models. In the present study, experimental data from Sautet et al. [15] and Wu et al. [16] were taken as a basis for non-reacting and reacting flows respectively. Benim et al. [17] referred to the same experimental setups within their 2D study, a schematic drawing of which is shown in Fig. 1. Via the flame tube, a mixture of hydrogen and nitrogen is issued into a hot co-flow at temperatures of  $T_{co} = 1010 \dots 1050$  K. The co-flow results from the combustion of a hydrogen-air mixture, which enters the setup through a perforated plate, consequently forming a matrix burner.

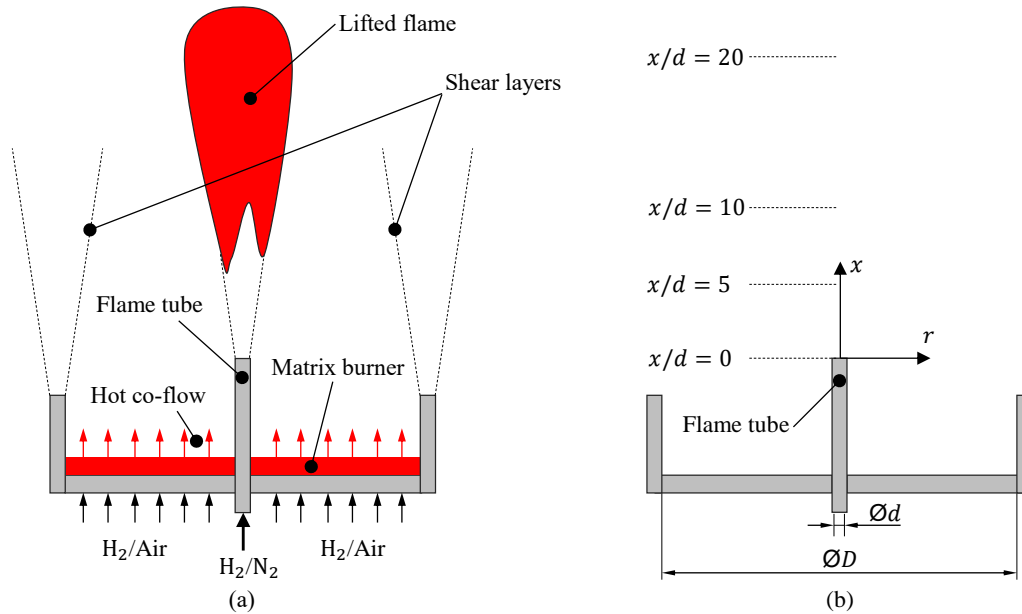


**Fig. 1** Experimental reference case setup, (a) lifted  $H_2/N_2$  flame in a preconditioned co-flow produced by a matrix burner, characteristic shear layers between co-flow and ambient air, (b) definition of coordinate system, flame tube inner diameter  $d$ , co-flow diameter  $D$ , several normalized axial distances  $x/d$

In order to obtain an easy-to-implement boundary condition for the numerical setup, the numerous small flames of the matrix burner are simplified to a homogeneously mixed co-flow that only consists of three species: gaseous water  $\text{H}_2\text{O}$  as the combustion product, inert nitrogen  $\text{N}_2$ , and unburned excess oxygen  $\text{O}_2$ . The composition varies according to the temperature that is to be provided for the lifted flame further downstream. As can be seen from Table 1, the water content rises as the matrix burner is fueled with more hydrogen to increase the resulting co-flow temperature.

**Table 1** Composition of the reacting-case co-flow for different co-flow temperatures  $T_{\text{co}}$  to be provided for the lifted flame further downstream, species volume fractions  $x_i$ , data from [17]

$T_{\text{co}}$ [K]	1010	1013	1020	1030	1040	1044	1050
$x_{\text{N}_2}$ [–]	0.7506	0.7505	0.7501	0.7495	0.7491	0.7489	0.7486
$x_{\text{O}_2}$ [–]	0.1489	0.1487	0.1483	0.1477	0.1470	0.1468	0.1464
$x_{\text{H}_2\text{O}}$ [–]	0.1005	0.1008	0.1016	0.1028	0.1039	0.1043	0.1050

As illustrated in Fig. 1 (a), for reacting flows typically a flame can be observed at a certain lift-off height  $H$  above the flame tube. The coordinate system origin is defined at the center position of its exit orifice, see Fig. 1 (b), 70 mm above the matrix burner. From there, axis  $x$  is spanning axially upwards, along with the main flow direction, and axis  $r$  radially outwards. The indications  $d$  and  $D$  refer to the flame tube inner diameter and the co-flow diameter respectively. Table 2 summarizes the characteristic parameters of both experimental reference setups in the context of this study. Several differences can be noticed between the non-reacting setup from Sautet et al. [15], where naturally no flame will be present, and the reacting-flow setup from Wu et al. [16]. Besides the setup dimensions, axial velocity  $U$ , temperature  $T$ , and composition  $x_i$  of fuel jet and co-flow are varied.

**Table 2** Characteristic parameters of experimental setups considered for non-reacting [15] and reacting [16] flow investigations, velocity in  $x$  direction  $U$ , temperature  $T$ , flame tube inner diameter  $d$ , co-flow diameter  $D$ , flow composition as species volume fractions  $x_i$ , see Table 1 for a detailed breakdown on reacting co-flow composition

		non-reacting flow		reacting flow	
		central jet	co-flow	central jet	co-flow
$d, D$	[mm]	10	112	4.57	190
$U$	[m/s]	45	4.5	110	4
$T$	[K]	300	300	317.5	1010 ... 1050
$x_{\text{H}_2}$	[–]	0.80	–	0.25	–
$x_{\text{N}_2}$	[–]	0.20	0.79	0.75	0.7506 ... 0.7486
$x_{\text{O}_2}$	[–]	–	0.21	–	0.1489 ... 0.1464
$x_{\text{H}_2\text{O}}$	[–]	–	–	–	0.1005 ... 0.1050

### III. Numerical Simulation

This section is divided into three parts. In the first one, an overview of the numerical setup describes the general mesh structure and boundary conditions. The second and third subsections present the simulation results for non-reacting and reacting flow respectively, after introducing the key features and definitions of the evaluation parameters used for the given situation. Within the conclusive comparison of the simulated flame lift-off heights, a total of six different chemical reaction mechanisms is featured.

#### A. Setup

Proceeding from the experimental reference case geometry, an adaptive numerical setup was created. Figure 2 (a) shows a representative segment of the geometry, including the boundary conditions applied. To model the shear layers depicted in Fig. 1, a velocity side inlet was used. Matching the evaluation metrics with the experimental reference data

(section III.B.2) allowed for the determination of the velocity magnitude. The central  $H_2/N_2$  jet was implemented as mass flow inlet. The same applies to the co-flow, broken down into a homogeneous stream of products from the lean premixed combustion of hydrogen and air as described in section II. In non-reacting cases an air co-flow was used instead, see also Table 2. The mesh structure to be seen in Fig. 2 (b) is characterized by areas with smaller cells where either mixing processes (Zone A) or flame development (Zone B) will occur during simulation. This refinement can be recognized in the typical cell size distribution, see Fig. 2 (c), which is discussed in more detail in the grid study (section III.B.5).

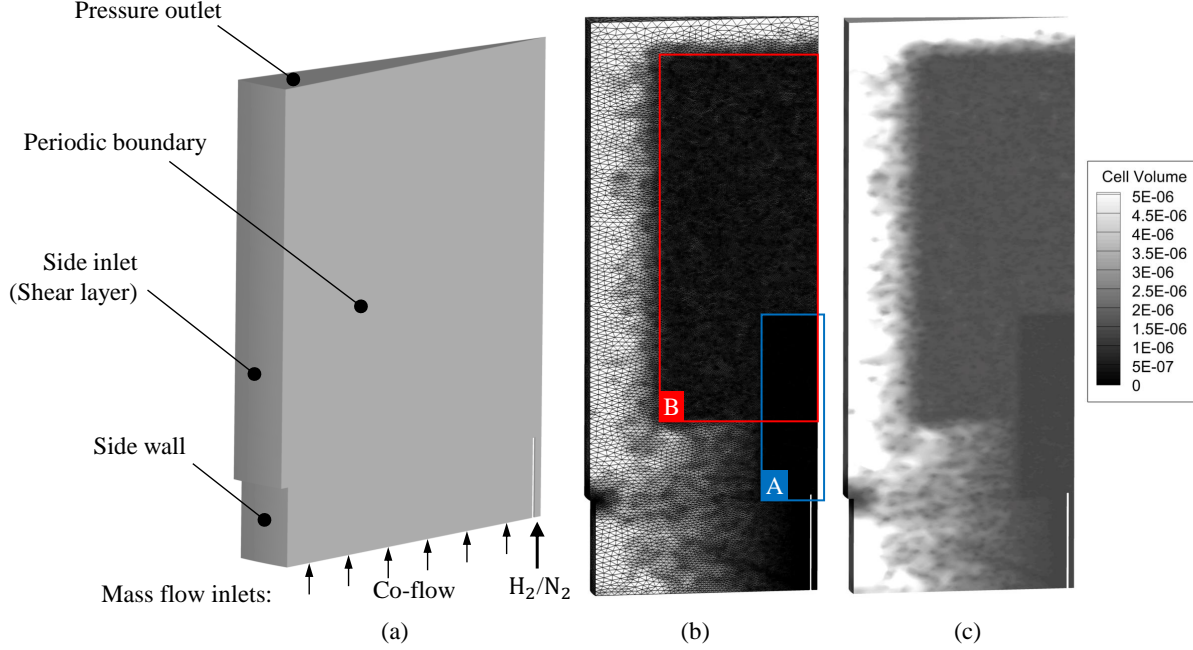


**Fig. 2 Numerical Setup, (a) boundary conditions on a representative  $10^\circ$  geometry segment, (b) general mesh structure, refined zones A for mixing and B for chemical reactions, (c) typical cell size distribution, volume in  $m^3$**

Geometry meshing and numerical simulations were performed using the commercial software environment ANSYS (version 2020/R1), that is ANSYS Fluent Meshing and the CFD code ANSYS Fluent. All calculations were based on a steady-state RANS approach with second order upwind schemes for spatial discretization and SIMPLE algorithm for pressure-velocity coupling. The influence of periodic model segmentation (section III.B.3) and different turbulence models (III.B.4) were studied in preparation for reacting-flow simulations. A convergence of the flow field solution was typically obtained after 200 000 iterations.

## B. Non-reacting Flow

Seeking to model the experimental boundary conditions sufficiently, the non-reacting flow field is analyzed without any chemical reactions taking place. This evaluation of the numerical model shall provide a validation basis prior to investigations on the reacting flow featuring hydrogen flames.

### 1. Model Evaluation

According to Sautet et al. [15], the fuel jet is axisymmetric and self-similar. Therefore, it can be described well by means of scalar quantities. The following evaluation parameters are used to allow for a comparison between simulation and experiment, referring to [15]: velocity half-value radius  $\delta$ , jet mean excess velocity  $\bar{U}_{ex}$ , and mixing density, divided into mean centerline density  $\bar{\rho}_{cl}$  and effective density  $\rho_{eff}$ .

The velocity half-value radius  $\delta$  is defined as the radial position  $r = \delta$ , where the mean axial velocity  $\bar{U}(x, \delta)$  falls below 50% of the centerline value  $\bar{U}(x, 0)$ . It is normalized with the flame tube inner diameter  $d$  to yield  $\delta/d$ . As illustrated by Fig. 3, the normalized velocity half-value radius is  $\delta/d \approx 0.5$  within the flame tube at  $x = 0$  and represents the fuel jet's opening after being issued into the co-flow.

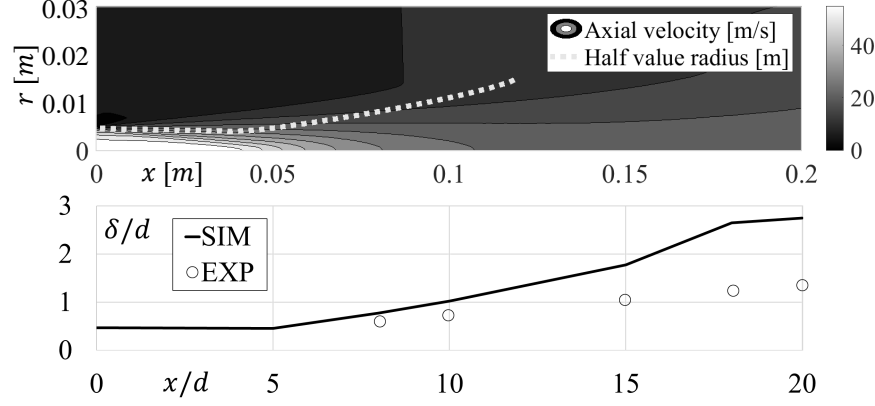


**Fig. 3** Axial velocity field of  $\text{H}_2/\text{N}_2$  jet issuing into the co-flow during a non-reacting simulation,  $d = 10$  mm, normalized velocity half-value radius  $\delta/d$ , comparison of simulation (SIM) with experimental (EXP) data [15]

The jet mean excess velocity  $\bar{U}_{\text{ex}}$  is defined by

$$\bar{U}_{\text{ex}} = \frac{\bar{U}(x, r) - \bar{U}(x, \infty)}{\bar{U}(x, 0) - \bar{U}(x, \infty)} = \frac{\bar{U} - U_{\infty}}{U_0 - U_{\infty}}, \quad (1)$$

with the local mean velocity  $\bar{U} = \bar{U}(x, r)$ , surrounding co-flow velocity  $U_{\infty} = \bar{U}(x, \infty)$  and corresponding mean axial velocity at the centerline  $U_0 = \bar{U}(x, 0)$ . As two indicators of the degree of mixing, representing the transition of the central jet into the co-flow, the mean centerline density  $\bar{\rho}_{\text{cl}}$  and the (approximated) effective density  $\rho_{\text{eff}}$  are defined as

$$\bar{\rho}_{\text{cl}}(x) = \bar{\rho}(x, 0) \quad (2)$$

and

$$\rho_{\text{eff}}(x) = \frac{\int_0^{\infty} \bar{\rho} \bar{U} (\bar{U} - U_{\infty}) dr^2}{\int_0^{\infty} \bar{U} (\bar{U} - U_{\infty}) dr^2}. \quad (3)$$

The undisturbed co-flow density  $\rho_{\infty} = \bar{\rho}(x, \infty)$  is used to create the normalized density parameters  $\bar{\rho}_{\text{cl}}/\rho_{\infty}$  and  $\rho_{\text{eff}}/\rho_{\infty}$ .

## 2. Side Inlet Velocity

In order to model the shear layers from Fig. 1, different side inlet velocities were applied to the velocity inlet boundary condition, described in Fig. 2. The results of model evaluation are depicted in Fig. 4 (a)–(d). For higher values of  $x/d$ , as the jet expands into the co-flow, the curves increasingly deviate from the experiment for higher side inlet velocities. As this holds for all four evaluation parameters, it is especially noticeable for the mean excess velocity  $\bar{U}_{\text{ex}}$  in Fig. 4 (b). By matching simulation results and experimental data, a side inlet velocity of  $0.01 \text{ m/s}$  was chosen for the boundary condition to reproduce the shear layers' effect on the flow.

## 3. Periodic Model Segmentation

For rotationally symmetric problems, a periodic model segmentation, as suggested in Fig. 2, can reduce the complexity and with that the computational effort. Figure 5 shows that a variation in segment size has a relatively small influence on the simulation results in this case, considering all model evaluation parameters. Therefore, in further simulations a reduction to the smallest of the investigated segment sizes  $10^\circ$  was chosen to save simulation time without significant quality losses.

## 4. Turbulence Modeling

Three turbulence models were investigated to determine their influence during non-reacting flow simulations. Compared to more complex turbulence models like SST or RSM, the  $k-\epsilon$  based variants excel in robustness and simplicity. Starting from the Standard  $k-\epsilon$  model, Realizable  $k-\epsilon$  and RNG  $k-\epsilon$  were considered, as Fig. 6 reveals. Both

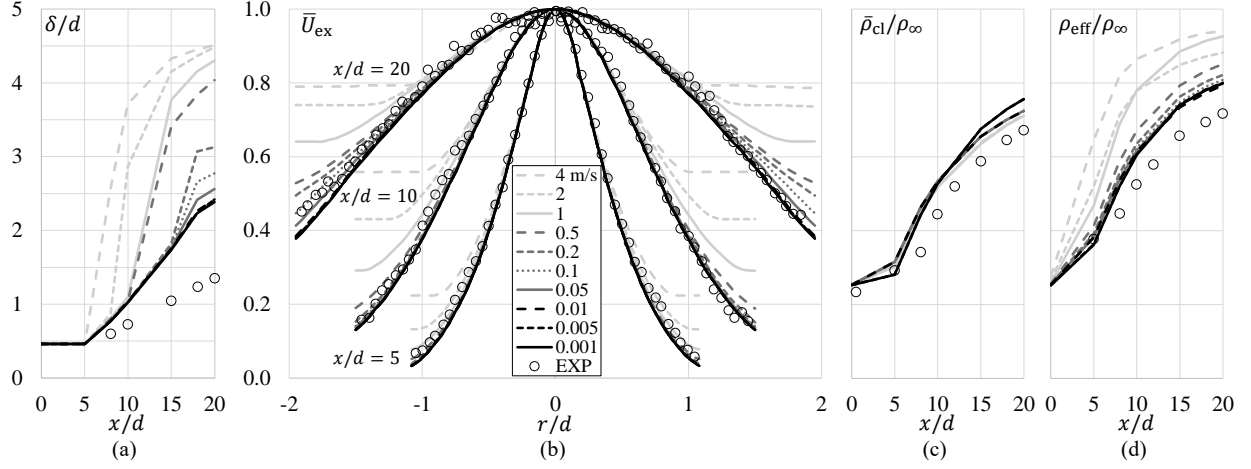


**Fig. 4** Determination of side inlet velocity: SIM and EXP [15] matching best for 0.01 m/s, influence on (a) velocity half-value radius  $\delta$ , (b) mean excess velocity  $\bar{U}_{ex}$ , (c) mean centerline density  $\bar{\rho}_{cl}$ , (d) effective density  $\rho_{eff}$

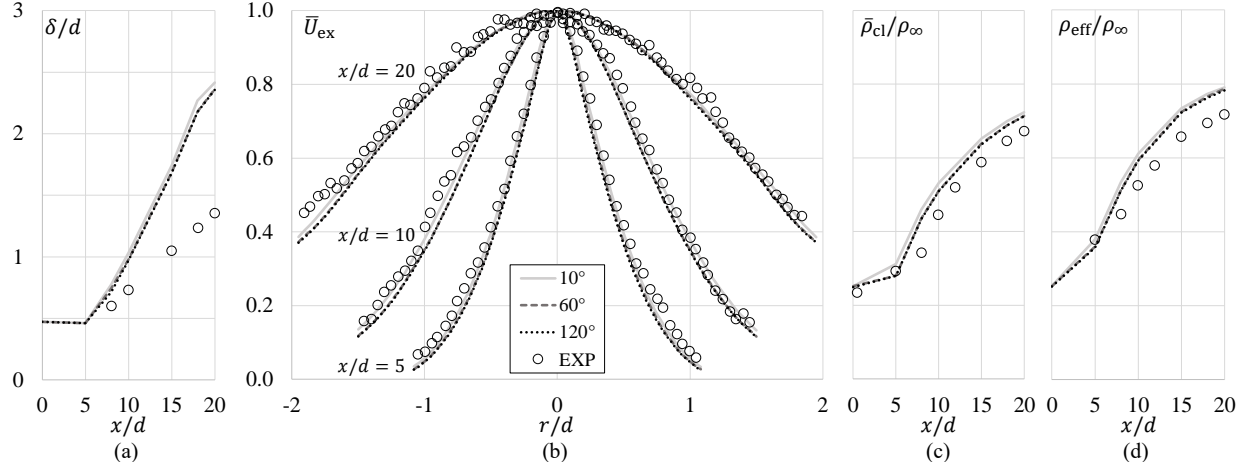


**Fig. 5** Comparison of different periodic model segmentations: no significant quality losses for smaller segment sizes, influence on (a) velocity half-val. rad.  $\delta$ , (b) mean exc. vel.  $\bar{U}_{ex}$ , (c) mean cent. dens.  $\bar{\rho}_{cl}$ , (d) eff. dens.  $\rho_{eff}$

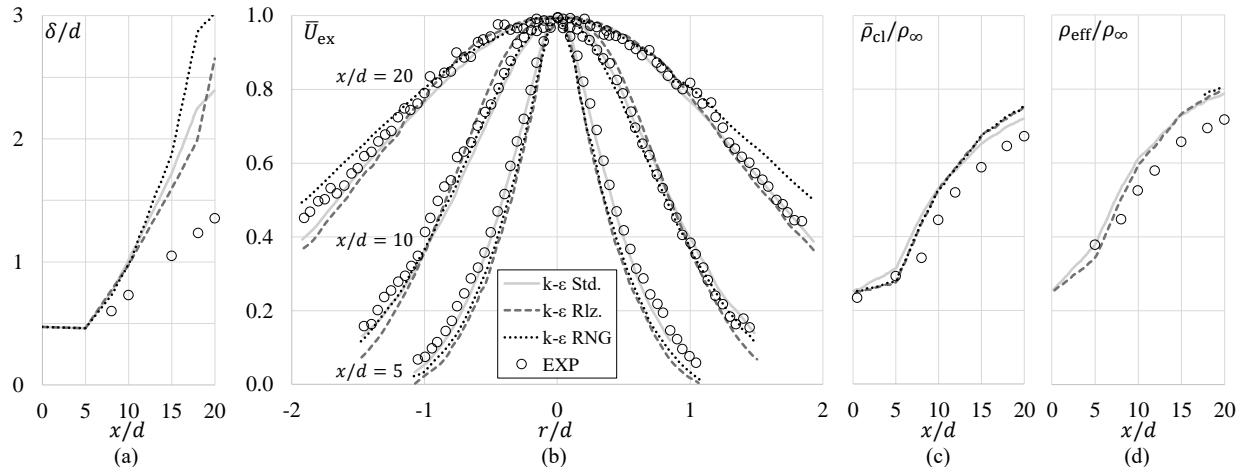


**Fig. 6** Comparison of different turbulence models: Standard / Realizable / RNG k- $\epsilon$ , best agreement for Standard k- $\epsilon$ , influence on (a) vel. HVR  $\delta$ , (b) mean exc. vel.  $\bar{U}_{ex}$ , (c) mean cent. dens.  $\bar{\rho}_{cl}$ , (d) eff. dens.  $\rho_{eff}$

of those extensions to the Standard  $k-\epsilon$  model can provide substantial improvements where flow features like strong streamline curvature, vortices and rotation occur. However, regarding the model evaluation parameters, for  $x/d > 10$  large deviations from the experiment can be observed for all turbulence models in Fig. 6. Since probably the flow only features moderate amounts of swirl in the present case, the Standard  $k-\epsilon$  model still shows the best overall agreement with the experimental data. Moreover, the Standard  $k-\epsilon$  model is associated with the lowest computational cost, which confirms its use in all simulations.

### 5. Grid Study

Retaining the grid macrostructure from Fig. 2, five different meshes investigated to perform a mesh independence study. An overview of total mesh sizes is shown in Table 3. Based on the reference case (VAL), which is used for the simulation of reactive flows in section III.C, two coarsened grids (C1, C2) and two refined grids (F1, F2) were derived. A factor of approximately 2 in the number of cells, nodes and faces separates the grid refinement levels from each other. The coarsest mesh C2 forms an exception from this rule. Referring to Fig. 2, outside of the refined zones A and B, the cell sizes equal those in mesh C1. The reduced number of cells within zones A and B leads to a relatively small difference in the total mesh size.

**Table 3 Overview of mesh sizes used for the grid study**

mesh name	C2	C1	VAL	F1	F2
cells	967 226	1 076 315	2 040 631	4 465 052	8 866 863
nodes	194 943	217 857	404 386	854 125	1 633 141
faces	1 939 118	2 157 487	4 088 982	8 939 771	17 745 908

In Fig. 7, the non-reacting flow simulation results of the five different mesh refinement levels are compared along with experimental data. Concerning velocity half-value radius  $\delta$  in Fig. 7 (a), all meshes show a qualitatively and quantitatively similar overprediction of the experiment. An analogous observation can be made for mean centerline density and effective density in Fig. 7 (c) and (d). A good overall agreement was reached for the mean excess velocity  $\bar{U}_{ex}$ , see Fig. 7 (b). No significant variations corresponding to the level of grid refinement were found. Accordingly, the reference level VAL was selected for the reacting-flow simulations.

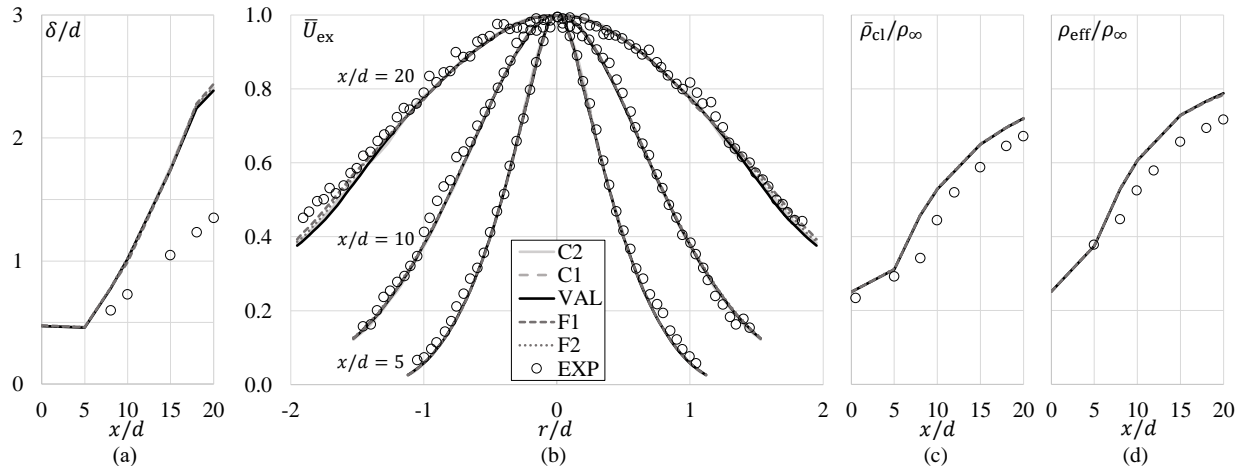


**Fig. 7 Grid study featuring five mesh refinement levels (C2, C1, VAL, F1, F2), experimental data (EXP) from [15], no significant differences, reference level VAL meets requirements, (a) velocity half-value radius  $\delta$ , (b) mean excess velocity  $\bar{U}_{ex}$ , (c) mean centerline density  $\bar{\rho}_{cl}$ , (d) effective density  $\rho_{eff}$**

### C. Reacting Flow

As next step after the non-reacting flow simulations, combustion models were included. To start combustion, the EDM was applied for 800 iterations, featuring one global reaction that produces water from hydrogen and oxygen. After switching to the EDC, at least 150 000 iterations were carried out to obtain convergence. Different chemical reaction mechanisms were used in combination with EDC, which resulted in a comparative study of lift-off heights depending on co-flow temperatures.

#### 1. Chemical Reaction Mechanisms

Table 4 gives an overview of six chemical reaction mechanisms that were investigated during the simulation of a lifted jet flame resulting from the combustion of hydrogen in a preconditioned co-flow. The mechanisms by Li et al. [18] and Ó Conaire et al. [19] are similar regarding the number of reactions for hydrogen and oxygen as well as the applicable ranges of temperatures, equivalence ratios and pressures. Keromnes et al. [20] originally designed and validated their mechanism for synthesis gas (syngas), exhibiting narrowed limits as against Li and Ó Conaire. Adding GRI-Mech 2.11 and GRI-Mech 3.0 [21] to the list, two less specific mechanisms in view of hydrogen combustion were taken into account. Although not optimized for hydrogen chemistry, GRI-Mech 3.0 can be considered partially validated for the stoichiometric combustion of hydrogen and air. Further increasing the variety of mechanisms covered by the recent 2D simulations from Benim et al. [17], besides GRI-Mech 3.0 the mechanism by Jachimowski [22] was included in the present study. It features a comparably broad temperature range as for Li and Ó Conaire, whereas equivalence ratio and pressure are more limited.

**Table 4 Summary of chemical reaction mechanisms investigated within this study, applicability limitations regarding the validated ranges of temperature  $T$ , equivalence ratio  $\Phi$  and pressure  $p$**

Mechanism	Species / Reactions	Applicability
Li et al. [18]	21 reactions for $H_2/O_2$	Flow reactor / Laminar premixed flames Shock tube measurements $T = 298 \dots 3000$ K, $\Phi = 0.25 \dots 5.0$ , $p = 0.3 \dots 87$ bar
Ó Conaire et al. [19]	19 reactions for $H_2/O_2$	Based on Mueller et al. $T = 298 \dots 2700$ K, $\Phi = 0.2 \dots 6.0$ , $p = 0.05 \dots 87$ bar
Keromnes et al. [20]	41 reactions for $H_2/CO/O_2/N_2/Ar$ mixtures	Designed for synthesis gas (syngas) $T = 914 \dots 2220$ K, $\Phi = 0.1 \dots 4.0$ , $p = 1 \dots 70$ bar
GRI-Mech 2.11 [21]	227 elementary reactions involving 49 species	Not optimized for $H_2/O_2/N_2$ chemistry $T = 900 \dots 1400$ K
GRI-Mech 3.0 [21]	325 elementary reactions involving 53 species 26 reactions for $H_2/O_2$	Optimized for Natural Gas, validated against experiments for ignition delay of stoichiometric $H_2$ /air mixtures at $p = 1$ bar and 2 bar
Jachimowski [22]	33 reactions for $H_2/O_2/N_2/Ar$ mixtures	Shock tube measurements $T = 670 \dots 2800$ K, $\Phi = 1.0 \dots 2.0$ , $p = 0.5 \dots 1.4$ bar

#### 2. Lift-off Height

The performance of different chemical reaction mechanisms is compared based on the lift-off height. Adhering to the definition by Benim et al. [17], the lift-off height  $H$  is calculated as the distance between the flame tube exit orifice at  $x = 0$  and the plane  $x = H$  cutting through the nearest point on the isotherm  $T_{iso} = T_{co} + 5$  K, where the local Favre-averaged temperature exceeds the co-flow temperature  $T_{co}$  by 5 K. This definition is illustrated by Fig. 8, showing the temperature field of reacting-flow simulations with the mechanism from Li et al. [18] activated. A variation in co-flow temperature and composition is featured for those values from Table 1 that allowed for converged simulation results. The corresponding isotherms are tagged accordingly for each case. A decreasing lift-off height can be observed as co-flow temperature increases.



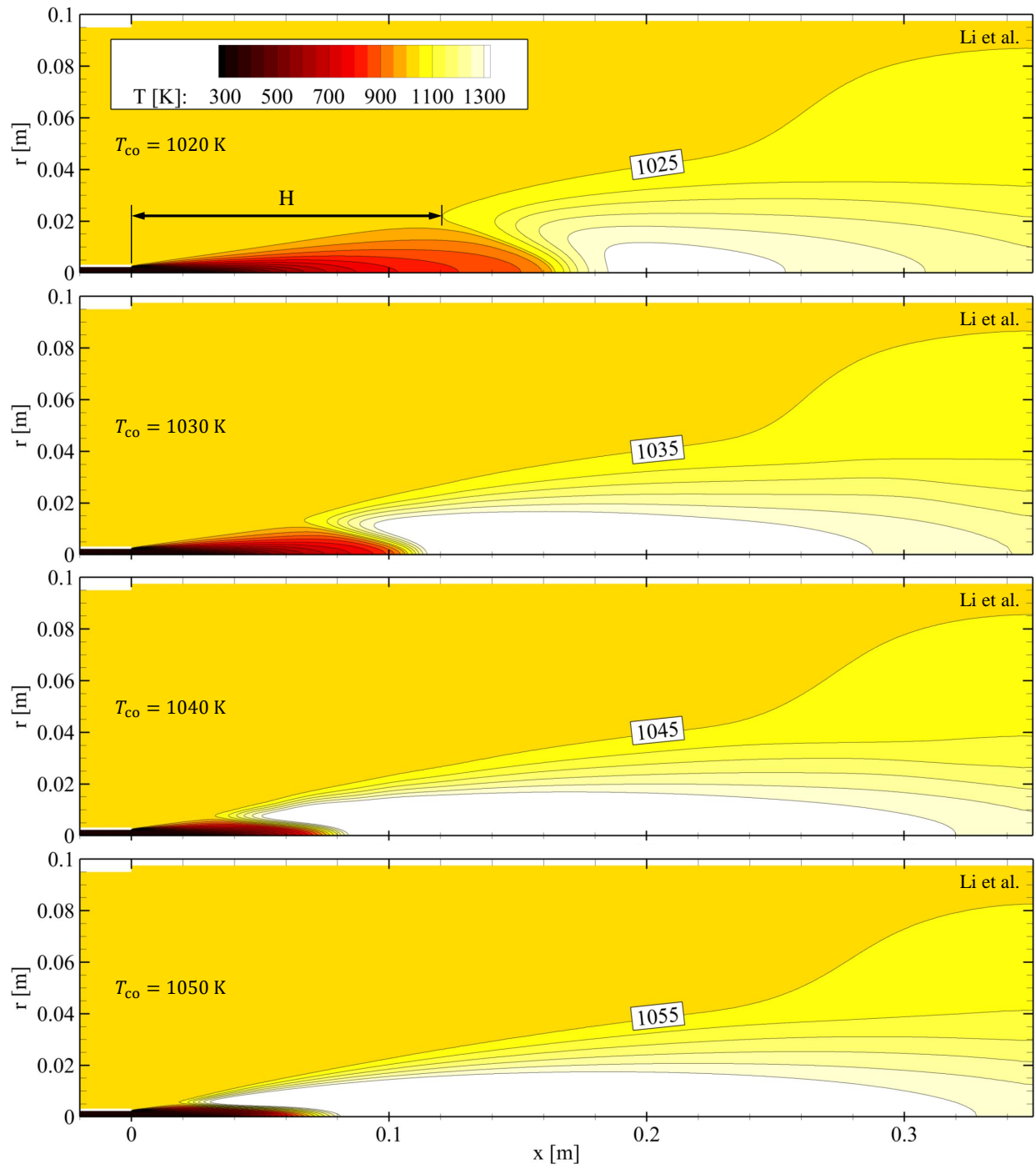


**Fig. 8** Temperature field for reacting flow, mechanism by Li et al. [18] applied, variation of co-flow temperature and composition according to Table 1, indication of flame lift-off height  $H$ , flame tube inner diameter  $d = 4.57$  mm

Figures 9 and 10 summarize the resulting lift-off heights for all chemical reaction mechanisms investigated over the co-flow temperature. A normalized lift-off height  $H/d$  is considered, referring to  $d = 4.57$  mm as the flame tube inner diameter for reacting-flow simulations, see Table 2. If available, the respective 2D simulation results from Benim et al. [17] are provided in each graph. Additionally, the measurements from Wu et al. [16] are taken as the experimental reference.

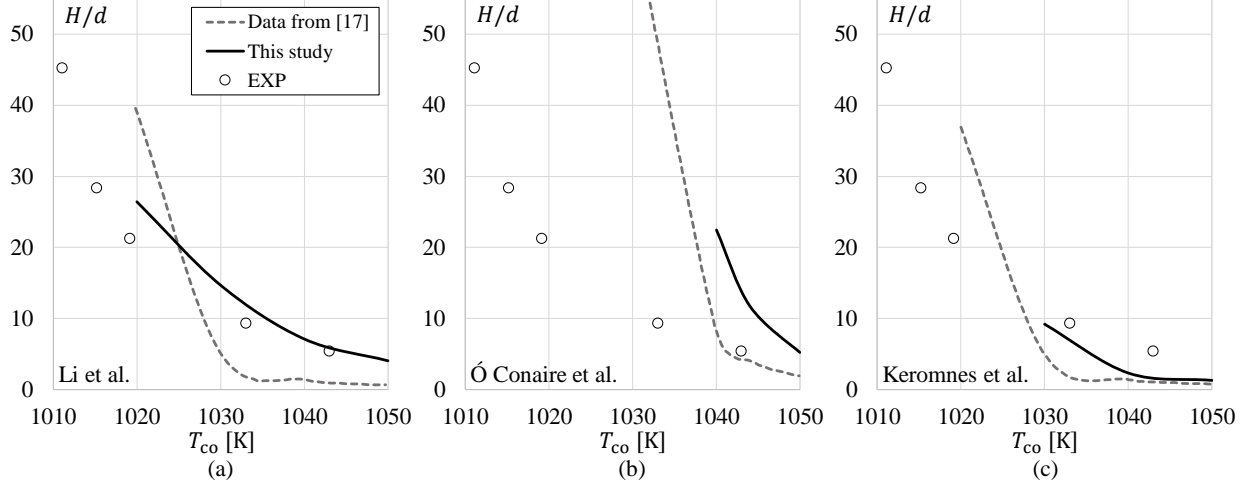


**Fig. 9** Normalized lift-off height over co-flow temperature applying reaction mechanism by (a) Li et al. [18], (b) Ó Conaire et al. [19], (c) Keromnes et al. [20]; 2D data from Benim et al. [17], EXP data from Wu et al. [16]

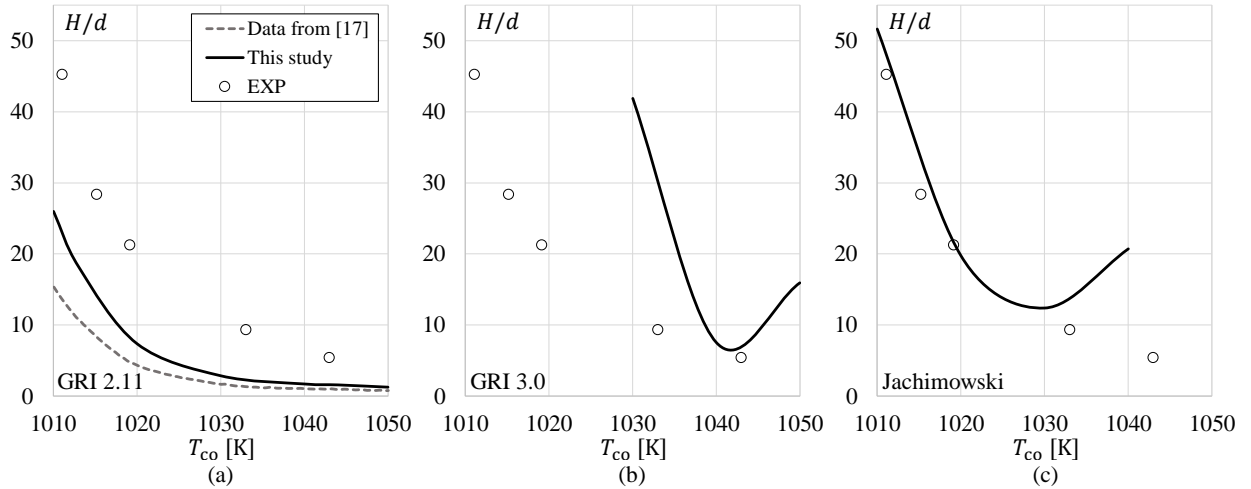


**Fig. 10** Normalized lift-off height over co-flow temperature applying reaction mechanism (a) GRI-Mech 2.11, (b) GRI-Mech 3.0 [21], (c) Jachimowski [22]; 2D data from Benim et al. [17], EXP data from Wu et al. [16]

The simulation results applying the mechanism by Li et al. are featured in Fig. 9 (a), showing the best agreement with measurements among all mechanisms investigated. This assessment is based on the combination of being able to reproduce the trend shown by the experimental values and simultaneously covering a large range of co-flow temperatures between  $T_{co} = 1020 \dots 1050$  K, within which stable simulation results could be obtained in this study. Still, the mechanism by Li et al. slightly overpredicts the lift-off height, especially for lower co-flow temperatures  $T_{co} \leq 1030$  K, transitioning into unstable simulation results below 1020 K. Compared to the 2D data from Benim et al. [17], a considerably better agreement with the experiment can be noticed.

Proceeding to the results for the mechanisms by Ó Conaire et al. and Keromnes et al. in Fig. 9 (b) and (c), the difference between the 2D simulation results and this study's 3D approach becomes visible again, depending on the

specific reaction mechanism used. Whereas for Ó Conaire the 3D results are even further off the experiment, they move closer for the Keromnes mechanism, although still underpredicting the experimental lift-off height. However, for both Ó Conaire and Keromnes the range of investigated co-flow temperatures is narrowed compared to the 2D case, with simulations already becoming unstable for  $T_{co} < 1040$  K and  $T_{co} < 1030$  K respectively.

Looking at GRI-Mech 2.11 in Fig. 10 (a), the comparison of 2D versus 3D results ends. A similar behavior can be recognized, with the 3D results lying closer to the experimental values while still significantly underpredicting the lift-off height. Like in Benim et al. [17], the GRI-Mech 2.11 was the only mechanism able to cover the same range of co-flow temperatures as in the corresponding experiments. Despite the quantitative deviations, the GRI-Mech 2.11 reflected the overall trend of the experimental data qualitatively well. As opposed to that, using GRI-Mech 3.0 resulted in a strong overprediction for co-flow temperatures other than  $T_{co} \approx 1040$  K, see Fig. 10 (b). The respective simulations were largely unstable and therefore difficult to perform or reproduce. A similar-looking curve shape, shifted towards lower co-flow temperatures, can be observed for the mechanism by Jachimowski in Fig. 10 (c). Whereas for temperatures  $T_{co} < 1030$  K a very good agreement with the experimental values is noticeable, lift-off height was overpredicted above 1030 K and simulations became increasingly unstable.

To gain an additional impression of the results for the mechanism by Jachimowski from Fig. 10 (c), several temperature fields of the reacting-flow simulations are shown in Fig. 11. The co-flow variation is featured by analogy with Fig. 8, including the respective isotherms. With increasing co-flow temperature, the lift-off height decreases until 1030 K and increases again afterwards. For  $T_{co} = 1030$  K the lift-off height seems greatly determined by a hot streak passing upstream, illustrating the limitations of assessing the performance based on the lift-off height as a single parameter. Furthermore, for the given boundary conditions in this study, the chemical reaction mechanisms were applied in an extremely lean combustion regime, pushing to the limits of their validity and beyond. Because of these unfavorable conditions, a lower overall prediction quality was already expected from the beginning and resulted in many simulations becoming unstable in the course of computation.

## IV. Conclusion

In the present study, a lifted  $H_2/N_2$  jet flame configuration has been analyzed to reinforce the foundation to further explore simulation methods for hydrogen combustion. A systematic study of the non-reacting flow field allowed for a validated numerical model to be employed for the reacting-flow simulations. The performance of six different chemical reaction mechanisms, all validated for hydrogen combustion, was assessed based on their capability to predict the experimental flame lift-off heights from Wu et al. [16].

Featuring 3D simulations with considerably higher mesh resolutions, this study constitutes a decisive extension to the available literature [17]. In particular, different turbulence models as well as chemical reaction mechanisms of various complexity were added to make the investigations more comprehensive. The recent 2D simulation results from Benim et al. [17] were included for discussion, while extending the scope of previous work. In summary, an overall better agreement of the presented 3D simulation results with the experimental values [16] was found. Among the chemical reaction mechanisms investigated, the one by Li et al. [18] gave the best results.

Particularly with regard to the limitations that were pointed out by this study, the numerical simulation of lifted flames involving hydrogen combustion still remains a challenging task. The quality of lift-off height prediction as such might not be the only focus, since also the applicability of this method for assessing the performance should be discussed more critically. By way of example, alternative evaluation methods could be considered as further research is needed to gain a more accurate understanding of the relationship between the complex hydrogen chemistry during combustion processes and corresponding combustion models for different chemical reaction mechanisms.

## References

- [1] Wüning, J., and Wüning, J., "Flameless oxidation to reduce thermal NO-formation," *Progress in Energy and Combustion Science*, Vol. 23, No. 1, 1997, pp. 81–94. [https://doi.org/10.1016/S0360-1285\(97\)00006-3](https://doi.org/10.1016/S0360-1285(97)00006-3).
- [2] Cavaliere, A., and de Joannon, M., "MILD Combustion," *Progress in Energy and Combustion Science*, Vol. 30, No. 4, 2004, pp. 329–366. <https://doi.org/10.1016/j.pecs.2004.02.003>.
- [3] M. de Joannon and A. Cavaliere and T. Faravelli and E. Ranzi and P. Sabia and A. Tregrossi, "Analysis of process parameters for steady operations in methane mild combustion technology," *Proceedings of the Combustion Institute*, Vol. 30, No. 2, 2005, pp. 2605–2612. <https://doi.org/10.1016/j.proci.2004.08.190>.

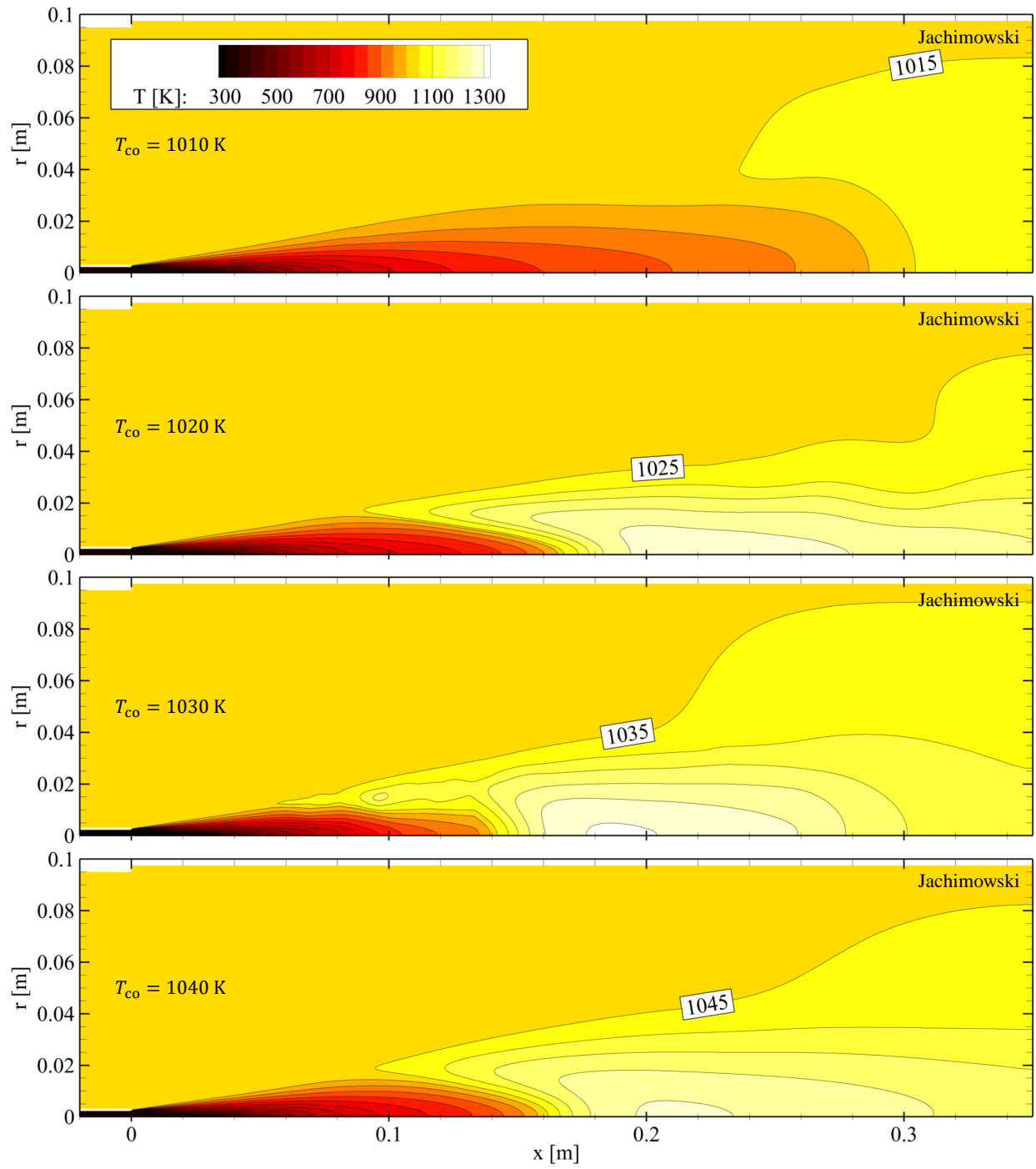


**Fig. 11** Temperature field for reacting flow, mechanism by Jachimowski [22] applied, variation of co-flow temperature and composition according to Table 1, flame lift-off height  $H$ , flame tube inner diameter  $d = 4.57$  mm

- [4] Mancini, M., Schwöppe, P., Weber, R., and Orsino, S., "On mathematical modelling of flameless combustion," *Combustion and Flame*, Vol. 150, No. 1, 2007, pp. 54–59. <https://doi.org/10.1016/j.combustflame.2007.03.007>.
- [5] Lückcrath, R., Meier, W., and Aigner, M., "FLOX<sup>®</sup> Combustion at High Pressure With Different Fuel Compositions," *Journal of Engineering for Gas Turbines and Power*, Vol. 130, No. 1, 2008. <https://doi.org/10.1115/1.2749280>.
- [6] Flamme, M., "Low NO<sub>x</sub> combustion technologies for high temperature applications," *Energy Conversion and Management*, Vol. 42, No. 15, 2001, pp. 1919–1935. [https://doi.org/10.1016/S0196-8904\(01\)00051-6](https://doi.org/10.1016/S0196-8904(01)00051-6).
- [7] Flamme, M., "New combustion systems for gas turbines (NGT)," *Applied Thermal Engineering*, Vol. 24, No. 11, 2004, pp. 1551–1559. <https://doi.org/10.1016/j.applthermaleng.2003.10.024>, industrial Gas Turbine Technologies.
- [8] Lammel, O., Stöhr, M., Kutne, P., Dem, C., Meier, W., and Aigner, M., "Experimental Analysis of Confined Jet Flames by Laser Measurement Techniques," 2011, pp. 117–127. <https://doi.org/10.1115/GT2011-45111>.
- [9] Yin, Z., Boxx, I., Stöhr, M., Lammel, O., and Meier, W., "Confinement-Induced Instabilities in a Jet-Stabilized Gas Turbine Model Combustor," *Flow, Turbulence and Combustion*, Vol. 98, 2017, pp. 217–235. <https://doi.org/10.1007/s10494-016-9750-5>.
- [10] Grimm, F., Lourier, J.-M., Lammel, O., Noll, B., and Aigner, M., "A Selective Fast Fourier Filtering Approach Applied to High Frequency Thermoacoustic Instability Analysis," 2017. <https://doi.org/10.1115/GT2017-63234>.
- [11] Lammel, O., Stöhr, M., Kutne, P., Dem, C., Meier, W., and Aigner, M., "Experimental Analysis of Confined Jet Flames by Laser Measurement Techniques," *Journal of Engineering for Gas Turbines and Power*, Vol. 134, No. 4, 2012. <https://doi.org/10.1115/1.4004733>.
- [12] Magnussen, B., and Hjertager, B., "On mathematical modeling of turbulent combustion with special emphasis on soot formation and combustion," 1977, pp. 719–729. [https://doi.org/10.1016/S0082-0784\(77\)80366-4](https://doi.org/10.1016/S0082-0784(77)80366-4).
- [13] Magnussen, B., "On the structure of turbulence and a generalized eddy dissipation concept for chemical reaction in turbulent flow," *AIAA 19th Aerospace Sciences Meeting, St. Louis, MO, U.S.A.*, 1981. <https://doi.org/10.2514/6.1981-42>.
- [14] Cabra, R., Myhrvold, T., Chen, J., Dibble, R., Karpetis, A., and Barlow, R., "Simultaneous laser Raman-Rayleigh-LIF measurements and numerical modeling results of a lifted turbulent H<sub>2</sub>/N<sub>2</sub> jet flame in a vitiated coflow," *Proceedings of the Combustion Institute*, Vol. 29, No. 2, 2002, pp. 1881–1888. [https://doi.org/10.1016/S1540-7489\(02\)80228-0](https://doi.org/10.1016/S1540-7489(02)80228-0).
- [15] Sautet, J., and Stepowski, D., "Dynamic behavior of variable-density, turbulent jets in their near development fields," *Physics of Fluids*, Vol. 7, 1995, pp. 2796–2806. <https://doi.org/10.1063/1.868658>.
- [16] Wu, Z., Stårner, S., and Bilger, R., "Lift-off heights of turbulent H<sub>2</sub>/N<sub>2</sub> jet flames in a vitiated co-flow," *Proceedings of the 2003 Australian Symposium on Combustion & The 8th Australian Flame Days, Monash University, Australia, Melbourne, Australia*, 2003.
- [17] Benim, A. C., and Pfeiffelmann, B., "Comparison of Combustion Models for Lifted Hydrogen Flames within RANS Framework," *Energies*, Vol. 13, No. 1, 2020, p. 152. <https://doi.org/10.3390/en13010152>.
- [18] Li, J., Zhao, Z., Kazakov, A., and Dryer, F. L., "An updated comprehensive kinetic model of hydrogen combustion," *International Journal of Chemical Kinetics*, Vol. 36, No. 10, 2004, pp. 566–575. <https://doi.org/10.1002/kin.20026>.
- [19] Ó Conaire, M., Curran, H. J., Simmie, J. M., Pitz, W. J., and Westbrook, C. K., "A comprehensive modeling study of hydrogen oxidation," *International Journal of Chemical Kinetics*, Vol. 36, No. 11, 2004, pp. 603–622. <https://doi.org/10.1002/kin.20036>.
- [20] Keromnes, A., Metcalfe, W., Heufer, K., Donohoe, N., Das, A., Sung, C.-J., Herzler, J., Naumann, C., Griebel, P., Mathieu, O., Krejci, M., Petersen, E., Pitz, W., and Curran, H., "An experimental and detailed chemical kinetic modeling study of hydrogen and syngas mixture oxidation at elevated pressures," *Combustion and Flame*, Vol. 160, No. 6, 2013, pp. 995–1011. <https://doi.org/10.1016/j.combustflame.2013.01.001>.
- [21] Bowman, C., Hanson, R., Davidson, D., Gardiner, W., Lissianski, V., Smith, G., Golden, D., Frenklach, M., and M., G., "GRI-Mech," *Gas Research Institute (2021)*, 2021.
- [22] Jachimowski, C., "Analytical study of the hydrogen-air reaction mechanism with application to scramjet combustion," *U.S. Department of Energy: Office of Scientific and Technical Information (1988)*, 1988.